WILEY | Hindawi

Research Article

A Blend of Analytical and Numerical Methods to Compute Orthogonal Image Moments over a Unit Disk

Manoj K. Singh,[1] Sanoj Kumar,[1] Gaurav Bhatnagar,[2] Deepika Saini,[3] Musrrat Ali,[4] Chandra Mani Sharma ⓘ,[5] and Navel Sharma ⓘ[6]

[1]*Department of Mathematics, University of Petroleum and Energy Studies, Dehradun, India*
[2]*Department of Mathematics, Indian Institute of Technology Jodhpur, India*
[3]*Department of Mathematics, Graphic Era (Deemed to Be) University, Dehradun, India*
[4]*Department of Basic Sciences, PYD, King Faisal University, Al Ahsa, Saudi Arabia*
[5]*CRDT, Indian Institute of Technology Delhi New Delhi, India*
[6]*Department of Computer Engineering & Informatics Academic City University College, Accra, Ghana*

Correspondence should be addressed to Chandra Mani Sharma; cmsharma.its@gmail.com
and Navel Sharma; drnavel.sharma@gmail.com

Accurate image moment computation is critical because they are used in a variety of fields, including image reconstruction and object recognition. Orthogonal polynomials are frequently used to compute moments due to their numerous intersecting and important theoretical properties. In polar coordinate systems, orthogonal polynomials such as the Polar Harmonic Fourier Transform (PHFT) and Polar Harmonic Transformation (PHT) are defined. However, the images are defined by a Cartesian coordinate system. To obtain image moments, a double integration over a unit circle over the product of the PHFT or PHT and the image function must be performed. The choice of double integration techniques and domain for the double integral has a significant effect on the precision of the computed moments. We have proposed a method for using the entire unit circle as an integration domain in this study, for image reconstruction. We used the PHFT and PHT to apply this technique to computing moments for the reconstruction. The proposed method outperforms other state-of-the-art methods, including Gaussian quadrature numerical integration method (GQM) and zeroth order approximation (ZOA) on variety of scenarios using three benchmarked image sets. We have demonstrated experimentally that this technique significantly improves the accuracy of image moments in higher order moments, as measured by reduced mean squared error (MSE). Additionally, the proposed method significantly improved the moment's rotational (an improvement of 1-3% as compared to GQM and an improvement of 37-93% as compared to ZOA) and scaling invariance (an improvement of 0-500% as compared to GQM and an improvement of 3-7000% as compared to ZOA).

1. Introduction

Image moments are important in many fields, including object recognition, image registration, robot navigation, image retrieval, watermarking, medical imaging, and forensic applications (Flusser and Zitová [1]; Liu et al. [2]; Zitová and Flusser [3]; Clemente et al. [4]; Hosny et al. [5]; Xu et al. [6]; Mostafa et al. [7]; Xin et al. [8]; Xin et al. [9]; Singh and Upneja [10]; Li et al. [11]; Hosny and Darwish [12]; Ma et al. [13]; Mahdian and Saic [14]). Image moments of a two-dimensional function defined over a compact domain (such as an image function) are defined as the double integration of its product with a two dimensional basis polynomial function (Flusser and Zitová [15]). Generally, as polynomial basis functions, products of some powers of two variables are taken, and in this case, the moment is known as the geometric moment (Flusser and Zitová [15]). If the basis functions are mutually orthogonal, the corresponding moment

is known as the orthogonal moment (Flusser and Zitová [15]). In a vector space, any element from a basis can be expressed as a linear combination of elements from another basis. Since we compute the integration in the discrete domain owing to the fact that the image function is discrete, the orthogonal basis provides a stable computation of the moments. In addition, orthogonal functions can be generated using recurrence relations, which allow computation of the moments without using the large powers of variables. Orthogonal image moments can be computed in various compact domains. For example, Legendre moments (Teh and Chin [16]) and Chebyshev moments (Mukundan et al. [17]) can be defined over the rectangular domain $[-1, 1] \times [-1, 1]$. Zernike moments (Xin et al. [8]; Xin et al. [9]), orthogonal Fourier–Mellin moments (Sheng and Shen [18]), polar complex exponential moments (Li et al. [11]), and polar harmonic Fourier moments (PHFM) (Wang et al. [19]) can all be defined over a unit disk, which is a subset in two-dimensional Euclidean space with each point less than or equal to unit distance from the origin.

Since its inception by Teague ([20]), the orthogonal set of moment functions defined over a circular region has been extensively studied. Due to the translation, rotation, and scaling invariance properties, the continuous orthogonal circular moments have found many applications, including image representation (Liu et al. [2]), forgery detection in duplicate objects (Hosny et al. [21]), vein recognition (Wang et al. [22]), breast cancer detection (Singh et al. [23]), SAR image classification (Gishkori and Mulgrew [24]), biomedical image retrieval (Kumar et al. [25]), and image watermarking (Xin et al. [8], Xin et al. [9]; Singh and Upneja [10]; Li et al. [11]; Hosny and Darwish [12]; Ma et al. [13]; Singh et al. [26]).

Computation of the moments with the orthogonal basis functions over circular domains involves the double integration of the product of the basis functions with the image function over the unit disk. The basis functions are defined over polar coordinates, while the image functions are defined over the rectangular coordinate system. To integrate, the two functions must be in the same coordinate system. Generally, the image function is transformed to a polar coordinate system before the integration. However, since the image function is discrete, only an approximate value of the moments can be computed. Therefore, an accurate algorithm for computing the moments is desirable. An image must be mapped over this domain to integrate over the entire unit disk. There are two methods for mapping the image: inscribed circle and circumscribed circle techniques (Wang et al. [19]; Ma et al. [13]). Since many applications, such as image watermarking techniques, require rotationally invariant moments and circumscribed circles are not capable of computing rotational invariant moments, we have followed the inscribed circle mapping technique in this paper. To integrate over the unit disk using discrete techniques, the unit disk must be gridded. There are two popular methods for gridding: polar grids (Xin et al. [8], Xin et al. [9]; Hosny and Darwish [12]) and rectangular grids (Li et al. [11]; Ma et al. [13]). The PHT moments computed using the polar grids are shown to be more accurate when

using the rectangular grids with a zeroth order approximation by Hosny and Darwish [12]. Prior to applying the integration, the image function needs to be transformed in the polar domain using interpolation techniques. In applications such as watermarking, interpolation needs to be done twice, once during the watermark embedding process, and another time during the watermark extraction process. This might deteriorate the performance of watermarking. Recently, Ma et al. [13] showed that the performance of watermarking in the rectangular domain using Gaussian numerical integration and PHFM is better than the performance of watermarking in the polar coordinate system using PHT moments. In addition, Singh et al. [26] showed that the performance of watermarking in the rectangular domain using blend of analytic and numerical approach and PHFM improves the watermarking ability of Ma et al. [13].

In the Cartesian coordinates, the image pixels, with their center falling within the unit circle, are taken for double integration. While there is no ambiguity for pixels completely falling within or outside the unit circle, there is enough ambiguity for pixels falling over the boundary of the circle. Some pixels are left out, and some are considered in the integration process. The moments are computed in many applications using this traditional method known as zeroth order approximation (ZOA) by Xin et al. [8], Xin et al. [9], and Li et al. [11]. More about the computation of moments in the Cartesian coordinate system is described in the methodology section. In the traditional method, which is a grid and summation method, and in the Gaussian quadrature numerical integration method (GQM) (Ma et al. [13]; Singh and Upneja [10]), the entire unit disk is not utilized for the moment computation. In the proposed work, we have used the combined analytic and numerical methods of Singh et al. [26] to utilize the entire unit disk for the moment computation and increase the accuracy of the computed moments. Multiple moments have been proposed for images, but there is a research gap on the moment computations. The novelty of the current work is to use the method presented in Singh et al. [26] for image reconstruction and providing a framework for exact moment computations for image reconstruction. The image processing community working in the image moments will get benefit from the framework. For example, the moments presented in Pawlak et al. [27], Wang et al. [28], and Wang et al. [29] can be computed by the framework. For demonstration of the efficiency of the method, we have selected four popular orthogonal moments defined over the unit disk, the PHFT and PHT families of moments, consisting of three types of orthogonal basis. We then compared the accuracy of the computed moments with the ZOA and the GQM techniques for image reconstruction. It is observed that the method has better accuracy for moment computations than existing methods discussed in this paper. It has been further shown that the moments computed by using this method are closer to the rotational and scaling invariance properties as compared to the existing methods. The PHFT and PHT moments over the unit disk are discussed in the next section. The double integration involved in the moment computations is presented in Section 3. The experimental results and discussion

are presented in Section 4, followed by the concluding remarks in Section 5.

2. Orthogonal Image Transform Moments

2.1. Polar Harmonic Fourier Transform Moments. The PHFT with order $u >= 0$ and repetition $v \in Z$, the set of integers, of a polar function $g(r, \phi)$ is a complex function defined over a unit disk by Wang et al. [19]:

$$C_{uv} = \frac{2}{\pi} \int_0^{2\pi} \int_0^1 H_{uv}(\bar{r}, \phi) g(r, \phi) r dr d\phi, \tag{1}$$

where,

$$H_{uv}(r, \phi) = T_u(r) e^{iv\phi}. \tag{2}$$

$T_u(r)$ is called the radial basis function and expressed as

$$T_u(r) = \begin{cases} \dfrac{1}{\sqrt{2}}, & \text{if } u = 0. \\ \sin{(u+1)\pi r^2}, & \text{if } u > 0 \text{ and } u \bmod 2 = 1 \\ \cos{u\pi r^2}, & \text{if } u > 0 \text{ and } u \bmod 2 = 0 \end{cases} \tag{3}$$

The functions $H_{uv}(r, \phi)$ form an orthogonal family of functions, i.e.,

$$\frac{2}{\pi} \int_0^{2\pi} \int_0^1 H_{u_1 v_1}(r, \phi) H_{u_2 v_2}(\bar{r}, \phi) r dr d\phi = 1 \text{ if } (u_1, v_1) = (u_2, v_2), \text{else } 0. \tag{4}$$

The polar function $g(r, \phi)$ (it can be an image function) can be reconstructed using the orthogonal property (Equation (4)) of PHFT moments by Wang et al. [19]:

$$g(r, \phi) = \sum_{u=0}^{umax} \sum_{v=-vmin}^{vmax} C_{uv} H_{uv}(r, \phi). \tag{5}$$

Here, *umax* is the maximum order of moments taken, and *vmax* is the maximum repetition taken for the reconstruction.

2.2. Polar Harmonic Transform Moments. The polar harmonic transform consists of three families of functions, polar complex exponential transform (PCET), polar cosine transform (PCT), and polar sine transform (PST). PCET with order u and repetition v (u and v are in set of integers) of a polar function $g(r, \phi)$ is a complex function defined over the unit disc as

$$C_{uv} = \frac{1}{\pi} \int_0^{2\pi} \int_0^1 H_{uv}(\bar{r}, \phi) g(r, \phi) r dr d\phi, \tag{6}$$

where,

$$H_{uv}(r, \phi) = e^{i\left(2\pi ur^2 + v\phi\right)}. \tag{7}$$

The functions $H_{uv}(r, \phi)$ with $u, v \in Z$, the set of integers, are orthogonal to each other, that is,

$$\frac{1}{\pi} \int_0^{2\pi} \int_0^1 H_{u_1 v_1}(r, \phi) H_{u_2 v_2}(\bar{r}, \phi) r dr d\phi = 1 \text{ if } (u_1, v_1) = (u_2, v_2), \text{else } 0. \tag{8}$$

PCT with order u and repetition v (u is in the set of non-negative integers and v is in the set of integers) of a polar function $g(r, \phi)$ is a complex function defined over the unit disc as

$$C_{uv}^c = \Omega_u \int_0^{2\pi} \int_0^1 H_{uv}^c(\bar{r}, \phi) g(r, \phi) r dr d\phi, \tag{9}$$

where,

$$H_{uv}^c(r, \phi) = \cos{(\pi ur^2)} e^{iv\phi},$$

$$\Omega_u = \begin{cases} \dfrac{1}{\pi}, & \text{if } u = 0 \\ \dfrac{2}{\pi}, & \text{if } u > 0 \end{cases}. \tag{10}$$

Similarly, PST with order u and repetition v (u is in the set of positive integers and v is in the set of integers) of a polar function $g(r, \phi)$ is a complex function defined over the unit disc as

$$C_{uv}^s = \Omega_u \int_0^{2\pi} \int_0^1 H_{uv}^s(\bar{r}, \phi) g(r, \phi) r dr d\phi, \tag{11}$$

where,

$$H_{uv}^s(r, \phi) = \sin{(\pi ur^2)} e^{iv\phi}. \tag{12}$$

Using the property given in Equation (8), we can reconstruct the polar function $g(r, \phi)$ (it can be an image function) as

$$g(r, \phi) = \sum_{u=-umin}^{umax} \sum_{v=-vmin}^{vmax} C_{uv} H_{uv}(r, \phi), \tag{13}$$

where *umin* in the case of PCT is 0, in the case of PST is 1, and in the case of PCET, we have taken *umin* = *umax*; here, *umax* is the maximum order of moments taken, and *vmax* is the maximum repetition taken for reconstruction. Equation (13) is reconstruction expression for the PCET. For reconstruction using PCT and PST, the function $H_{uv}(r, \phi)$ should be replaced with $H_{uv}^c(r, \phi)$ and $H_{uv}^s(r, \phi)$, respectively.

3. Methodology

Let us consider a square image $f(x, y)$ of size $N \times N$, $x, y = 0, 1, \cdots, N - 1$. Since the domain of the PHFT and PCT moments is unit disk, the image must be first transformed into the unit disk. In the inscribed circle method, the pixel coordinates are linearly scaled to $[-1\ 1]$. Consider first the x-coordinate of the pixel. The values $x = 0, 1, \cdots, N$ represent the left and right boundaries of the pixels as an equation of straight line perpendicular to the x-axis. The x-coordinates are scaled to $[-1\ 1]$ using the linear relation $x' = -1 + (2x/N)$. The width of the pixel δx can be computed by subtracting boundaries of pixels. That is,

$$\delta x = -1 + \frac{2(x+1)}{N} - \left(-1 + \frac{2x}{N}\right) = \frac{2}{N}. \qquad (14)$$

Therefore, the x-coordinates of the center of each pixel in the unit disk will be $cx_i = -1 + (2i/N) + (1/N)$, $i = 0, 1, \cdots N - 1$. Similarly, $\delta y = 1/N$ and the y-coordinates of the center of pixels in the unit disk will be $cy_j = -1 + (2j/N) + (2/N)$, $j = 0, 1, \cdots N - 1$. With these notations, the PHFT in discrete polar coordinates can be defined as

$$C_{uv} = \frac{2}{\pi} \sum_i \sum_j f(i, j) H_{uv}\left(\overline{cx}_i, cy_j\right) \delta x \delta y, \qquad (15)$$

where i, j runs over all pixels on the unit disk. In the simplest form, Equation (15) can be approximated with the following equation:

$$C_{uv} = \frac{8}{N^2 \pi} \sum_i \sum_j f(i, j) H_{uv}\left(\overline{cx}_i, cy_j\right), \qquad (16)$$

where i, j are runs over indices with restriction on (cx_i, cy_j) that they must be within and on the unit disk. This simplification for computing the moments is known as the zeroth order approximation.

The accuracy of the computed moment can be increased by extending the $H_{uv}(\overline{cx}_i, cy_j) \delta x \delta y$ term as

$$H_{uv}\left(\overline{cx}_i, cy_j\right) \delta x \delta y = \int \int H_{uv}(\overline{r}, \phi) r dr d\phi. \qquad (17)$$

Here, the domain of integration is the rectangular domain $[cx_i - (\delta, x/2)cx_i + (\delta, x/2)] \times [cy_j - (\delta, y/2)cy_j + (\delta, y/2)]$ with restriction that the polar point (r, ϕ) must be in the unit disk. The accuracy of the moments depends on the computation of the double integral in Equation (17). Several approaches for the approximation of the integration have been proposed in the literature. The function H_{uv} is a function of the polar coordinates. However, in Equation (15), the function corresponding to the image, $f(x, y)$, is a piecewise continuous function of the Cartesian coordinates x and y. Therefore, to find the moments using Equation (15), either the function $f(x, y)$ should be transformed to the polar coordinate system or the function H_{uv} should be

transformed to the Cartesian system. In the former case, Xin et al. [8] and Xin et al. [9] proposed a method for double integration over polar coordinates for accurate computation of the Zernike moments. Similarly, Hosny and Darwish [12] used the circular grids for the computation of PHTs. In this method, the unit circular region is gridded in polar domain, and the function $f(x, y)$ is interpolated over the circular domain. In this paper, we have focused on integration of kernel function over the Cartesian system. In this system, the circular domain is divided into non-over lapping grids. In Xin et al. [8] and Xin et al. [9], the authors have used the same rectangular grids (i.e., the zeroth order approximation) in computing Zernike and pseudo Zernike moments. Li et al. [11] used similar rectangular grids for computation of polar harmonic moments. The moments are further used for the application on image watermarking. In the absence of analytical method, the numerical method is used for the approximate evaluation of a definite integral. In the rectangular grid, Equation (17) can be approximated to

$$H_{uv}\left(\overline{cx}_i, cy_j\right) = \sum_{p=1}^{n_1} \sum_{q=1}^{n_2} H_{uv}\left(\overline{x}_p, y_q\right), \qquad (18)$$

where (x_p, y_q) are $n_1 \times n_2$ points taken in the neighborhood $[cx_i - (1/N)cx_i + (1/N)] \times [cy_j - (1/N)cy_j + (1/N)]$ with the restriction that (x_p, y_q) are within and on the unit disk. Xin et al. [8] and Xin et al. [9] used this simplified form for the computation of Zernike moments and pseudo Zernike moments using $n_1 = n_2 = 1$ (Equation (16) is a particular case of Equation (18) with $n_1 = n_2 = 1$). In this form of integration in the Cartesian coordinates, only the rectangular grids with centers falling within and on the unit circle are only considered, and the rectangular grids partially falling within the unit disk but centers outside the unit circle are neglected. This leads to the inaccuracies in the moment computation. The resulting inaccuracies and types of rectangular grids are discussed later in this section. This method requires the evaluation of the kernel function in each of the $n_1 \times n_2$ grids. Integration techniques involving polynomial interpolation can be used for increasing the accuracy of the integration with reduced number of function evaluation. Singh and Upneja [10] used the Gaussian quadrature integration method (GQM) in which Legendre polynomials are used for the approximation of the integration. In this technique, the moment computation takes the form in the following equation:

$$H_{uv}\left(\overline{cx}_i, cy_j\right) = \sum_{p=1}^{n_1} \sum_{q=1}^{n_2} w_p w_q H_{uv}\left(\overline{cx}_i + t_p/N, cy_j + t_q/N\right), \qquad (19)$$

where $(cx_i + t_p/N, cy_j + t_q/N)$ are $n_1 \times n_2$ points taken in the neighborhood $[cx_i - (1/N)cy_i + (1/N)] \times [c_j - (1/N)c_j + (1/N)]$ with restriction that they are within and on the unit circle. Here, w_p represents weights associated with the point inside a rectangular grid corresponding to t_p. The sum of

w_p is close to 2. Ma et al. [13] used this technique for computing the PHFT moments.

However, the condition that the sum of the w_is is close to two is violated at the grid elements intersecting with the circle. The points inside a grid are distributed symmetrically with respect to the center. All the points in a grid intersecting with the circle boundary are not considered for the integration. The points falling outside the circle are neglected. Therefore, the weights will not sum to 2. Figure 1 shows the representation of the unit circle over an image with a size of 16×16. The white colored pixels are completely inside the circle and the black colored pixels are completely outside the circle. The colored pixels (pixels barring black and white) represent the boundary of the circle. While using Equation (18), the integration is performed over the whole pixel if the center falls within the circular region and is completely ignored when the center falls outside the circle. We have used the analytical method to integrate the function over the pixel even if it is partially intersected with the unit circle. We have performed the double integration in each pixel separately. If a pixel is intersected by the circle partially, we have used the integration boundary as the circle, instead of a rectangular boundary. To integrate this analytic double integration we have used *dblquad* in *scipy* library. We call this moment computation method as QuadPack Method (QPM). The *dblquad* function takes input as the function to integrate and the limits of the double integration. For a pixel falling completely within the circle, the limits for the integration are constants, i.e., the boundaries of the rectangular domain. When a pixel is intersected by the unit circle, one of the limits is the equation of the unit circle ($x^2 + y^2 = 1$).

In summary, we used Equation (16) to compute the image moments. Here, the moments are defined based on the kernel function $H(.,.)$. We computed the kernel function using Equation (17). The image is reconstructed with PHT moments using Equation (13) and PHFT moments using Equation (5).

The moment computation is implemented in python3 and executed over two systems. One is an Ubuntu system with 8 GB RAM and four cores of 2.00 GHz. Another is a Windows 10 system with 8 GB RAM and four cores of 2.30 GHz. Since the moment's execution is computationally intensive, we have used *joblib* library for executing the code in parallel by using all the four cores. If we assume the integrand function to be constant and equal to 1, then the double integral of the function is the area of the domain over which we seek the integration. Therefore, for the double integration over the unit circle, the integration on the constant function with value one must be π. Figure 2 shows the comparison of the approximated π with the two algorithms. Since at $n = 7$, the GQM method is approximately close with π; we selected $n = 7$ for the comparison of our method with GQM and ZOA.

Theoretically, C_{00} of PCET must be constant k for constant image function $f(x, y) = k$. We have tested the three algorithms for $k = 172$. Using the ZOA, we computed the value of c_{00} as 172.099; using the GQM, we computed this
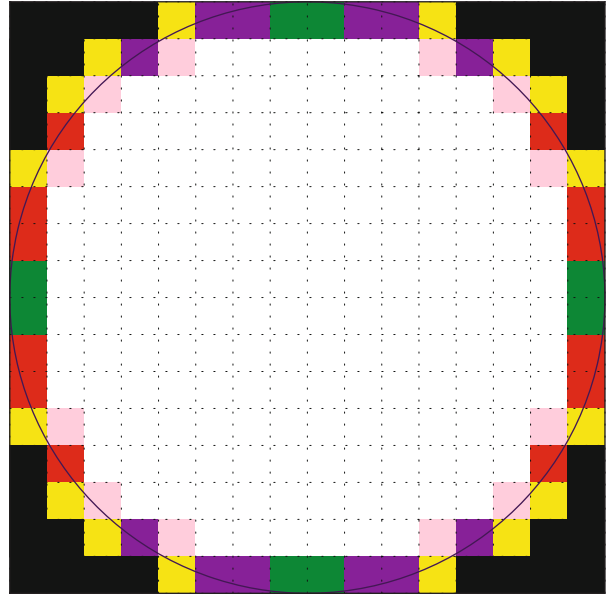

FIGURE 1: Representation of a unit circle over a 16×16 image. The white colored pixels are completely inside the circle, and the black colored pixels are completely outside the circle. Red colored pixels represent the intersection with circle at top and bottom, purple colored pixels represent the intersection with circle at left and right. Yellow colored pixels represent the intersection with circle at left and bottom. Pink colored pixels represent the intersection with circle at top and right. Green colored pixel represents the pixels where the circle is relatively parallel and close to one of the four boundaries.

value as 171.999; the proposed algorithm computes the c_{00} as 172.002. All the three algorithms perform equally well at this property. Theoretically, the c_{uv} with $u \neq 0$ and $v \neq 0$ must be zero. However, the computation of moments with $v = 4l, l \neq 0$ are not accurate and resulted in non-zero values. In particular, we computed $c_{04} = 0.0433$, applying the traditional method, $c_{04} = 0.0072$ using the Gaussian method and $c_{04} = 0.0022$ by applying the method presented in this paper. Therefore, the current method looks more accurate in the moment computations as far as constant function is concerned.

4. Experimental Result and Discussions

In this section, we will analyze the accuracy of the computed moments using the proposed method. We will compare the performance of the method with other two methods, ZOA and GQM. For measuring the accuracy of the moments, we have used image reconstruction using Equations (5) and (13). We have applied the method for computing moments over four orthogonal moments: PHFM, PCET, PCT, and PST. Three test images from diverse backgrounds are also selected for the study (Figure 3). One is the famous Lena image, another is a logo, and the third is a medical image.

4.1. PHFM. Figure 4 shows reconstruction of images using the three algorithms. The first row is reconstructed using
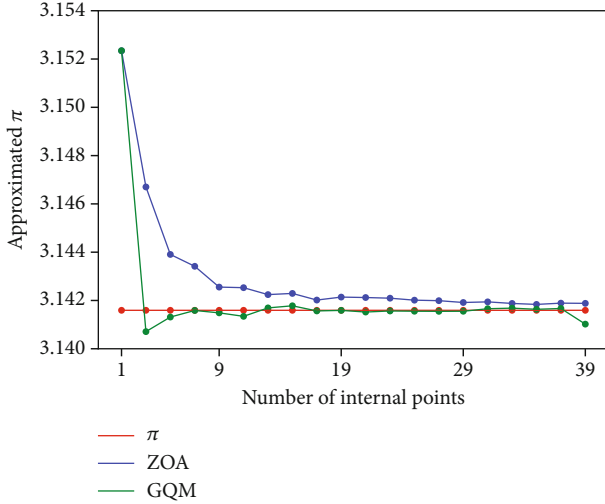
FIGURE 2: approximation of π using integration of unit function over unit circle using three algorithms.

ZOA, the second row is reconstructed using the GQM, and the third row is reconstructed using the QPM. The first two columns correspond to the reconstructed Lena image using moments and repetitions 0-20 and 0-100, respectively. Similarly, the next two columns correspond to the reconstructed Logo image using moments and repetitions 0-20 and 0-100, respectively. And the last two columns correspond to the reconstructed medical image using moments and repetitions 0-20 and 0-100, respectively. It is apparent from the figure that at low maximum order (0-20) for reconstruction, the three algorithms look similar with each other for all the three images. However, at higher maximum order (0-100) for reconstruction, the superiority of the GQM over the ZOA and the superiority of the QPM over the other two algorithms is apparent. At higher maximum moments, white patches appear at the center and the edges of the reconstructed image in first rows in all the three images. In the second row, the white patches at the center are clearly apparent in all the three images. The last row, which represents the image reconstruction using our method, clearly looks better than the reconstructed images using the other two algorithms in all the three images. Statistically, the reconstructed images are compared using the mean squared reconstruction error (MSE, ϵ), structural similarity index (SSIM), and feature similarity index (FSIM). The MSE is defined as

$$\epsilon = \frac{\sum_{i,j}(f(i,j) - g(i,j))^2}{\sum_{i,j}f(i,j)^2}, \qquad (20)$$

where f and g represents the original image and the reconstructed image, respectively. The indices i, j runs over the pixels within the unit circle. The MSE is average of the square of the difference of the origin image and reconstructed image. Therefore, the small values in the MSE indicate good reconstruction of the image, while the large values in the MSE indicate a large difference in the original image

and the reconstructed image. SSIM is the second statistics used to measure similarity between the images (Wang et al. [30]). It is relying on the fact that human visual system is highly adapted to extract the structural properties from images. FSIM is the third statistics used to measure similarity between the images (Zhang et al. [31]). It is relying on the fact that the human visual system primarily understands images based on the low level features. The local structures can be measured with the phase congruency. In FSIM, phase congruency is used as primary feature. The range of the SSIM and FSIM is 0-1. The high values in SSIM and FSIM represent a high similarity between the images, while the low values represent a low similarity between the images.

Table 1 shows the MSE, SSIM, and the FSIM between the base images and the reconstructed images. At low orders (0-20), the MSE, SSIM, and FSIM in all the three images across the algorithms are similar. Overall, at smaller order image reconstruction, the performance of all the three algorithms across images is at par with each other. The performance of the ZOA improves for the logo image. At high orders (0-60), the reconstruction quality of Lena and medical images drops in terms of MSE but increased in terms of SSIM and FSIM using the ZOA moments. However, in the logo, opposite effects appear as MSE decreased, but an increase in SSIM and FSIM was observed. The reconstruction qualities of both the other algorithms, GQM and QPM, have shown improvement in terms of all the three statistical parameters across the three images, as MSE drops significantly and SSIM and FSIM increased significantly. At orders (0-60), statistically, the quality of reconstructed images is better using GQM and QPM as compared to ZOA. However, between GQM and QPM, no one outperformed the other. At orders (0-100), the quality of reconstructed image using ZOA has decreased in terms of all the three statistics when compared with moment orders 0-60. The distinction between the performance of GQM and QPM is also apparent, as the MSE of QPM is smallest and SSIM is largest among the three methods across the three images. With the exception of the medical image where FSIM of QPM is comparable with GQM, the FSIM of QPM is largest among the three algorithms. Therefore, using Figure 4 and Table 1, we conclude that our method outperformed the other two methods across the three images.

If an image is rotated with an angle α, then the modified moments (c_{uv}^{α}) can be defined in terms of the moment (c_{uv}) of the original image as the following equation:

$$c_{uv}^{\alpha} = e^{-iv\alpha}c_{uv}. \qquad (21)$$

Therefore, $|c_{uv}^{\alpha}| = |c_{uv}|$, that is the absolute value of a moment, is invariant under rotation. Since we compute moments of an image in discrete domain, the achievement of the exact rotational invariant image moments is difficult, however. To show the variation in the moments with rotation in the image, we have computed the moments of the image at 9 different angles (10°, 20°, 30°, 40°, 50°, 60°, 70°, 80°, and 90°), counterclockwise direction. In addition to the QPM technique, we have also analyzed the variability
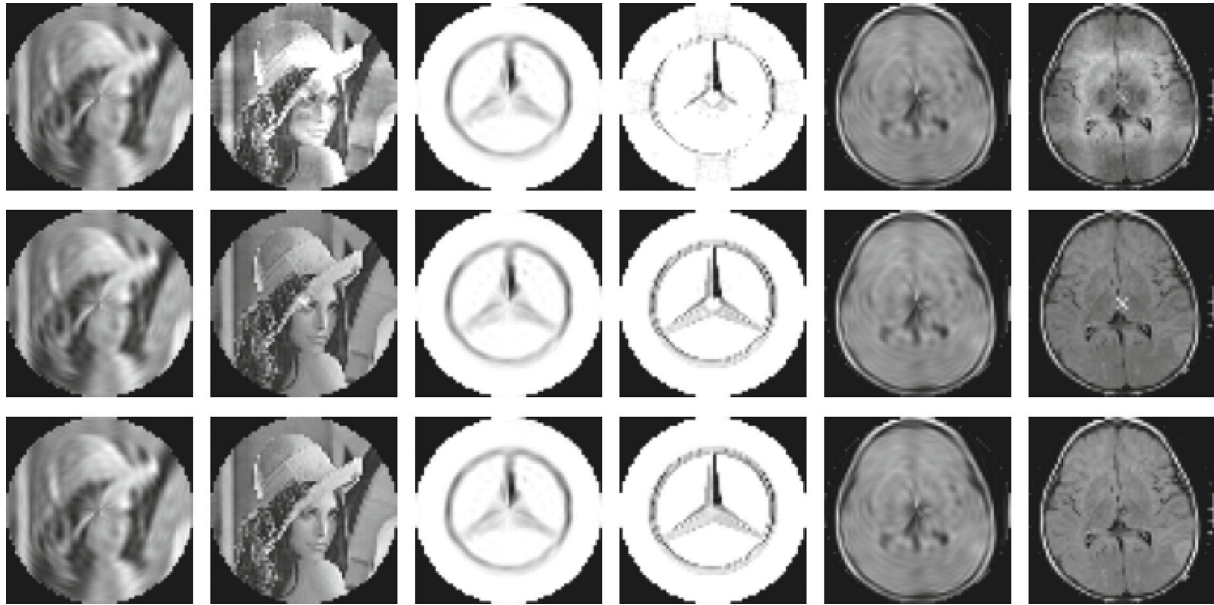
FIGURE 3: Test images taken for the study.

FIGURE 4: Reconstruction of image using PHFM with the three algorithms. The first row is reconstructed using the ZOA, the second row is reconstructed using the GQM, and the third row is reconstructed using the QPM. The first two columns correspond to the reconstructed Lena image using moments and repetitions 0-20 and 0-100, respectively. Similarly, the next two columns correspond to the reconstructed Logo image using moments and repetitions 0-20 and 0-100, respectively. And the last two columns correspond to the reconstructed medical image using moments and repetitions 0-20 and 0-100, respectively.

TABLE 1: MSE, SSIM, and FSIM between base images and reconstructed images. In columns 3-5, the images are reconstructed using orders 0-20 and repetition 0-20; in columns 6-8, the images are reconstructed using orders 0-60 and repetition 0-60; and in columns 9-11, the images are reconstructed using orders 0-100 and repetition 0-100. The first and second columns represent the images and algorithms, respectively, used for the reconstruction of the images.

| PHFM | | Maximum order 20 | | | Maximum order 60 | | | Maximum order 100 | | |
Image	Method	MSE	SSIM	FSIM	MSE	SSIM	FSIM	MSE	SSIM	FSIM
	ZOA	0.0227	0.8171	0.9101	0.0379	0.9123	0.9237	0.0853	0.8513	0.8978
Lena	GQM	0.0228	0.8154	0.9105	0.0035	0.9779	0.9861	0.0038	0.9825	0.9879
	QPM	0.0228	0.8155	0.9104	0.0034	0.9783	0.9857	0.0017	0.9904	0.9911
	ZOA	0.0054	0.8784	0.9469	0.0042	0.8629	0.9342	0.0055	0.8197	0.9242
Logo	GQM	0.0054	0.8791	0.9448	0.0008	0.9827	0.9878	0.0007	0.9868	0.9904
	QPM	0.0054	0.8789	0.9448	0.0006	0.9849	0.9897	0.0003	0.9941	0.9958
	ZOA	0.0271	0.7493	0.9007	0.0360	0.8240	0.9297	0.1372	0.7539	0.8791
Medical	GQM	0.0279	0.7466	0.8989	0.0057	0.9605	0.9711	0.0050	0.9677	0.9774
	QPM	0.0279	0.7468	0.8987	0.006	0.9554	0.9665	0.0030	0.9751	0.9777

of the moments using the ZOA and the GQM. We have used the mean squared error (MSE) between the absolute values of the original images and rotated images. The MSE for absolute moments at angle α is defined as

$$\sum_{u=0}^{100}\sum_{v=0}^{100}\left(|c_{uv}| - |c_{uv}^{\alpha}|\right)^2. \qquad (22)$$

Table 2 shows the MSE for absolute moments between the base images and rotated images. There is a definite pattern in all the images and algorithms. Between 10° and 90°, the MSE increases with an increase in angle, but after crossing the midway mark, the MSE starts decreasing. At 90°, there is no difference in the absolute values of the moments. The moments computed using the ZOA show larger MSE as compared to GQM and QPM. In all the three images, the MSE of the QPM is the smallest. Therefore, it can be concluded that our method matches best with the rotation invariance property among the three methods across the three images.

We have also tested the scaling invariance of the image moments. Table 3 shows MSE of the computed moments with two sizes of the images, when images are scaled to 0.75 (size = 48×48) and when images are scaled to 1.25 (size = 80×80). We observed that at size 48×48, the MSE is larger than MSE at size 80×80, in all the three algorithms and three images. In watermarking applications, it is shown that the orthogonal moments such as PHFM and PCET behave better when the scaling factor is greater than 1 (Ma et al. [13]; Hosny and Darwish [32]; Li et al. [11]). Therefore, this behavior of moments is in line with previous studies. The absolute values of the moments are larger at lower moments and smaller at higher moments. Therefore, for a reasonable accurately computed moment, the MSE at lower moments should be high, and at higher moments, it must be low, which is apparent with GQM and QPM. However, we noted that with ZOA, this behavior is opposite, indicating that the accuracy of the moments at higher order is not at all par with GQM and QPM. This is again consistent with Figure 4, where it was observed that at higher moments, the reconstructed images have large white patches. In the logo and medical images with size 48×48, the MSE of the QPM is larger than GQM at 0-20 order moments. However, at 80-100 order moments, the superiority of the QPM method is clearly observed. At the image with size80×80, our method outperformed all other methods as MSE is smaller than both the methods across the three images. Therefore, we see that the QPM method closely follows the scaling invariance. Overall, we observed that the QPM has a better reconstruction quality and shows a better invariance in rotation and scaling.

4.2. PCET. Figure 5 shows the reconstruction of images using the three algorithms applied on PCET. Similar to PHFM, the first row is reconstructed using ZOA, the second row is constructed using the GQM, and the third row is constructed using the QPM. The first two columns correspond to the reconstructed Lena image using moments and repeti-

tions 0-20 and 0-100, respectively. Similarly, the next two columns correspond to the reconstructed Logo image using moments and repetitions 0-20 and 0-100, respectively. And the last two columns correspond to the reconstructed medical image using moments and repetitions 0-20 and 0-100, respectively. It is apparent from the figure that at the low maximum order (0-20) for reconstruction, the three algorithms look similar with each other for all the three images. However, at higher maximum order (0-100) for reconstruction, the superiority of the GQM over the ZOA and the superiority of the QPM over the other two algorithms are apparent, as in the case of PHFM. Similar to PHFM, at higher maximum moments, the white patches appear at the center and the edges of the reconstructed image in the first rows in all the three images. In the second row, the white patches at the center are clearly apparent in all the three images. However, the white patches along the edges look more apparent as compared to PHFM. The last row, which represents the image reconstruction using our method, clearly looks better than the reconstructed images using other two algorithms in all the three images in the PCET moment. As compared with PHFM moments, the medical images reconstructed using PCET moments appear a little darker. Similarly, the edges of the logo also appear a little extended in the PCET moments as compared to PHFM.

Table 4 shows the MSE, SSIM, and the FSIM between the base images and the reconstructed images using PCET moments. A similar observation as in Table 1 can be made with Table 4. Here, we analyzed the key difference of the PCET moments with the PHFM moments. We observed that PCET moments have higher MSE across the table compared to the corresponding MSE of the PHFT moments. Here, we are not claiming that the performance of the PHFT is better than PCET. The two moments have a different support. As Table 1 is constructed using only positive moments (the PHFT is only defined for positive moments), Table 4 is constructed using both the negative and positive moments. The objective of this study is not the comparison of the PCET and PHFT. Here, we are comparing our method with ZOA and GQM on various orthogonal moments such as PHFT, PCET, PCT, and PST. Unlike the PHFT, in the PCET image reconstruction, we note that the performance of our method is superior without any ambiguity at the higher moments (0-100).

Table 5 shows the MSE for absolute moments between base images and rotated images. The analysis for this table is similar to the analysis of the Table 2. Here, we bring the main difference between the effects of rotation on the moments computed using the PHFM and the PCET. We noted that the MSE between the absolute moments between the base images and the rotated images is smaller in PCET as compared to the PHFM across algorithms. Therefore, the rotational invariance is supported in a stronger way in the PCET. At 90°, there is no difference in the absolute values of the moments. In all the three images, the MSE of the QPM is smallest. Therefore, it can be concluded that our method matches best with the rotation invariance among the three methods when applied on the PCET moments.

TABLE 2: MSE between absolute values of moments of base images and rotated images.

Image	Method	10°	20°	30°	40°	50°	60°	70°	80°	90°
	ZOA	0.0171	0.0195	0.0220	0.0244	0.0267	0.0237	0.0205	0.0170	0.0
Lena	GQM	0.0093	0.0102	0.0123	0.0149	0.0169	0.0137	0.0110	0.0092	0.0
	QPM	0.0091	0.0101	0.0122	0.0149	0.0168	0.0135	0.0109	0.0091	0.0
	ZOA	0.0147	0.0169	0.0196	0.0236	0.0236	0.0197	0.0177	0.0156	0.0
Logo	GQM	0.0101	0.0116	0.0140	0.0166	0.0164	0.0135	0.0117	0.0105	0.0
	QPM	0.0099	0.0116	0.0139	0.0165	0.0164	0.0134	0.0116	0.0102	0.0
	ZOA	0.0129	0.0152	0.0176	0.0198	0.0191	0.0167	0.0146	0.0128	0.0
Medical	GQM	0.0087	0.0103	0.0123	0.0145	0.0138	0.0117	0.0101	0.0085	0.0
	QPM	0.0087	0.0102	0.0122	0.0144	0.0137	0.0116	0.0100	0.0085	0.0

TABLE 3: MSE of absolute moments when image is scaled to various sizes (first column). The second column represents the order of the moments taken for comparison. The range of v in all the cases is between 0 and 20.

PHFM Size	u	ZOA	Lena GQM	QPM	ZOA	Logo GQM	QPM	ZOA	Medical GQM	QPM
48×48	0–20	0.0321	0.0322	0.0313	0.0518	0.0439	0.0442	0.1196	0.1139	0.1142
80×80	0–20	0.0144	0.0113	0.0111	0.0226	0.0177	0.0174	0.0660	0.0510	0.0509
48×48	80–100	0.0798	0.0075	0.0033	0.2504	0.0230	0.0035	0.0348	0.0016	0.0010
80×80	80–100	0.0614	0.0034	0.0032	0.2139	0.0047	0.0033	0.0240	0.0010	0.0009
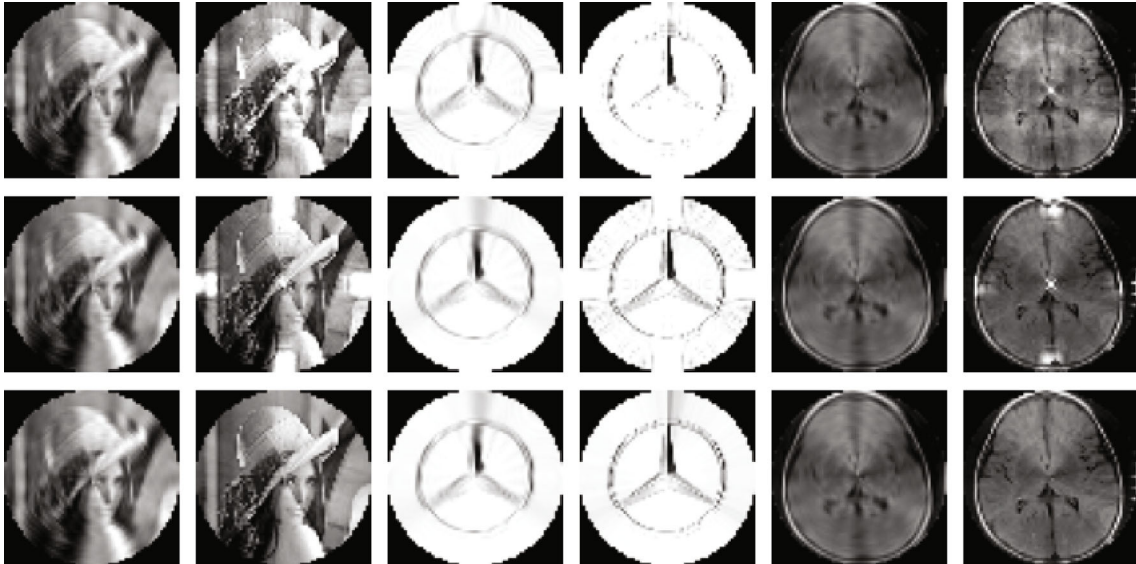
FIGURE 5: Reconstruction of image using PCET with the three algorithms. The first row is reconstructed using the ZOA, the second row is reconstructed using the GQM, and the third row is reconstructed using the QPM. The first two columns correspond to the reconstructed Lena image using moments and repetitions 0-20 and 0-100, respectively. Similarly, the next two columns correspond to the reconstructed Logo image using moments and repetitions 0-20 and 0-100, respectively. And the last two columns correspond to the reconstructed medical image using moments and repetitions 0-20 and 0-100, respectively.

Table 6 shows MSE of the computed moments with two sizes of the image, when the image is scaled to 0.75 (size = 48×48) and when the image is scaled to 1.25 (size = 80×80). We observed that at size 48×48, the MSE is larger than MSE at size 80×80, in all the three algorithms and three images with the exception of QPM at higher moments. In the image with size 48×48, the MSE of the QPM and GQM at 0-20 order moments are similar across images. However, at 80-100 order moments, the superiority of the QPM method is clearly observed. At the image with

TABLE 4: MSE, SSIM, and FSIM between the base images and reconstructed images using PCET moments. In columns 3-5, the images are reconstructed using orders 0-20 and repetition 0-20; in columns 6-8, the images are reconstructed using orders 0-60 and repetition 0-60; and in columns 9-11, the images are reconstructed using orders 0-100 and repetition 0-100. The first and second columns represent the images and algorithms, respectively, used for the reconstruction of the images.

PCET Image	Method	Maximum order 20			Maximum order 60			Maximum order 100		
		MSE	SSIM	FSIM	MSE	SSIM	FSIM	MSE	SSIM	FSIM
	ZOA	0.0530	0.7945	0.8751	0.0850	0.8351	0.8752	0.1040	0.8218	0.8715
Lena	GQM	0.0480	0.8053	0.8888	0.0352	0.9016	0.9307	0.0946	0.8254	0.8502
	QPM	0.0480	0.8055	0.8888	0.0345	0.9038	0.9315	0.0339	0.9107	0.9325
	ZOA	0.0064	0.8196	0.9129	0.0073	0.7897	0.9164	0.0087	0.7758	0.9304
Logo	GQM	0.0069	0.8402	0.9323	0.0041	0.9014	0.9514	0.0056	0.8141	0.8870
	QPM	0.0069	0.8403	0.9323	0.0041	0.9045	0.9543	0.0037	0.9167	0.9585
	ZOA	0.0563	0.7502	0.8700	0.0862	0.7450	0.8531	0.1272	0.7082	0.8425
Medical	GQM	0.0532	0.7508	0.8708	0.0387	0.8577	0.9074	0.1171	0.7785	0.8489
	QPM	0.0532	0.7513	0.8710	0.0388	0.8543	0.9043	0.0364	0.8632	0.9084

TABLE 5: MSE between absolute values of moments of base images and rotated images using PCET moments.

Image	Method	10°	20°	30°	40°	50°	60°	70°	80°	90°
	ZOA	0.0049	0.0059	0.0067	0.0072	0.0079	0.0071	0.0062	0.0050	0.0
Lena	GQM	0.0032	0.0047	0.0049	0.0057	0.0065	0.0055	0.0039	0.0028	0.0
	QPM	0.0024	0.0028	0.0033	0.0039	0.0044	0.0036	0.0029	0.0025	0.0
	ZOA	0.0041	0.0048	0.0055	0.0064	0.0064	0.0055	0.0049	0.0043	0.0
Logo	GQM	0.0027	0.0031	0.0037	0.0042	0.0042	0.0036	0.0031	0.0028	0.0
	QPM	0.0026	0.0031	0.0036	0.0042	0.0041	0.0035	0.0030	0.0027	0.0
	ZOA	0.0035	0.0040	0.0046	0.0052	0.0050	0.0045	0.0039	0.0034	0.0
Medical	GQM	0.0032	0.0038	0.0045	0.0047	0.0047	0.0042	0.0036	0.0030	0.0
	QPM	0.0022	0.0026	0.0030	0.0036	0.0034	0.0029	0.0025	0.0022	0.0

TABLE 6: MSE of absolute PCET moments when the image is scaled to various sizes (first column). The second column represents the order of the moments taken for comparison. Range of v in all the cases is between 0 and 20.

PCET Size	u	Lena			Logo			Medical		
		ZOA	GQM	QPM	ZOA	GQM	QPM	ZOA	GQM	QPM
48×48	0–20	0.0340	0.0148	0.0147	0.109	0.0159	0.0159	0.0157	0.0325	0.0326
80×80	0–20	0.0203	0.0070	0.0069	0.0601	0.0087	0.0086	0.0099	0.0157	0.0157
48×48	80–100	0.0656	0.0720	0.0005	0.2134	0.2151	0.0003	0.0241	0.0307	0.0001
80×80	80–100	0.0312	0.0696	0.0005	0.1011	0.2207	0.0004	0.0095	0.0152	0.0001

size 80×80, our method outperformed all other methods as MSE is very small cross the three images. Therefore, we see that the QPM method very closely follows the scaling invariance. Overall, we observed that the QPM has a better reconstruction quality and shows better invariance in rotation and scaling in PCET as well.

4.3. PCT. Figure 6 shows reconstruction of images using the three algorithms. Visually, the reconstructed images using the PCT look similar to that of PHFM. It is apparent from the figure that at low maximum order (0-20) for reconstruction, the three algorithms look similar with each other for all the three images. However, at higher maximum order (0-

100) for reconstruction, the superiority of the GQM over the ZOA and the superiority of the QPM over the other two algorithms are apparent. At higher maximum moments, the white patches appear at the center and the edges of the reconstructed image in first rows in all the three images. In the second row, the white patches at the center are clearly apparent in all the three images, similar to that of PHFM. The last row, which represents the image reconstruction using our method, clearly looks better than the reconstructed images using other two algorithms in all the three images.

Table 7 shows the MSE, SSIM, and the FSIM between the base images and the reconstructed images using PCT
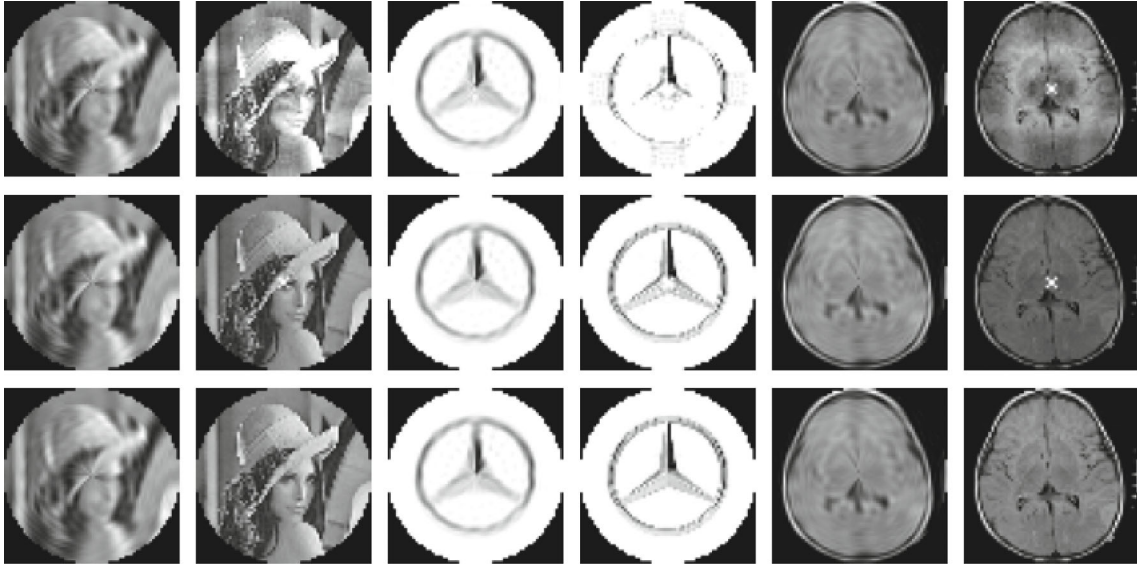
FIGURE 6: Reconstruction of image using PCT with the three algorithms. The first row is reconstructed using the ZOA, the second row is reconstructed using the GQM, and the third row is reconstructed using the QPM. The first two columns correspond to the reconstructed Lena image using moments and repetitions 0-20 and 0-100, respectively. Similarly, the next two columns correspond to the reconstructed Logo image using moments and repetitions 0-20 and 0-100, respectively. And the last two columns correspond to the reconstructed medical image using moments and repetitions 0-20 and 0-100, respectively.

TABLE 7: MSE, SSIM, and FSIM between the base images and reconstructed images using PCT moments. In columns 3-5, the images are reconstructed using orders 0-20 and repetition 0-20; in columns 6-8, the images are reconstructed using orders 0-60 and repetition 0-60; and in columns 9-11, the images are reconstructed using orders 0-100 and repetition 0-100. The first and second columns represent the images and algorithms, respectively, used for the reconstruction of the images.

PCT		Maximum order 20			Maximum order 60			Maximum order 100		
Image	Method	MSE	SSIM	FSIM	MSE	SSIM	FSIM	MSE	SSIM	FSIM
	ZOA	0.0201	0.8348	0.9173	0.0403	0.9118	0.9264	0.0911	0.8444	0.8946
Lena	GQM	0.0202	0.8331	0.9175	0.0028	0.9807	0.988	0.0044	0.9816	0.9882
	QPM	0.0202	0.8331	0.9175	0.0024	0.9822	0.9886	0.0012	0.9923	0.9923
	ZOA	0.0045	0.8915	0.9565	0.0042	0.8644	0.9393	0.0061	0.8017	0.9168
Logo	GQM	0.0045	0.8933	0.9581	0.0008	0.9822	0.9906	0.0006	0.9872	0.9913
	QPM	0.0045	0.8935	0.9582	0.0006	0.9851	0.9924	0.0002	0.9946	0.9966
	ZOA	0.0205	0.8086	0.9356	0.0384	0.8287	0.9446	0.1537	0.7482	0.8886
Medical	GQM	0.0212	0.8051	0.9342	0.0047	0.9709	0.9858	0.0108	0.9668	0.9789
	QPM	0.0212	0.8062	0.9344	0.004	0.9792	0.9881	0.0018	0.9886	0.9927

moments. We observed that the PCT moments have a similar MSE across the table compared to the corresponding MSE of the PHFT moments, as Tables 1 and 7 are constructed using same positive moments. We observed that at lower moments, the performance of all the three algorithms are at par with each other across the three images. At lower moments (0-20) of the first column of Table 7, the reconstructed image using PCT looks better than the reconstructed image using PHFM, as the MSE is smaller and SSIM and FSIM are larger in the PCT. The largest change is observed in the medical image, where the FSIM has increased from 0.74 to 0.80. At order (0-60), the performance of our algorithm is better than the other two algorithms in all the three images, as MSE is the smallest and

FSIM is the largest in our method. The SSIM is also better in our method, except in the medical image where the SSIM is slightly lower than GQM. At moment order (0-100), our method outperformed the other two methods. We noted that the PCT moments with our method have the best SSIM and FSIM when compared with PHFM and PCET. The FSIM and SSIM in the medical image are 0.98 and 0.99, respectively.

Table 8 shows the MSE for absolute moments between base images and rotated images. We noted that the entries corresponding to the MSE in Table 8 are larger than that of the entries in Table 5. The entries corresponding to the SSIM and FSIM in Table 8 are smaller than that of the entries in Table 5. Therefore, the rotational invariance

Table 8: MSE between absolute values of moments of base images and rotated images using PCT moments.

Image	Method	10°	20°	30°	40°	50°	60°	70°	80°	90°
	ZOA	0.0177	0.0204	0.0227	0.0251	0.0267	0.0238	0.021	0.0178	0.0
Lena	GQM	0.0096	0.011	0.013	0.0154	0.0167	0.0137	0.0115	0.0097	0.0
	QPM	0.0094	0.0108	0.0129	0.0153	0.0165	0.0135	0.0113	0.0095	0.0
	ZOA	0.0153	0.0173	0.0202	0.0246	0.0253	0.0213	0.0185	0.0163	0.0
Logo	GQM	0.0105	0.0119	0.0146	0.0171	0.0173	0.0145	0.0122	0.0111	0.0
	QPM	0.0103	0.0119	0.0145	0.0169	0.0173	0.0145	0.0122	0.0108	0.0
	ZOA	0.0129	0.0149	0.0175	0.0194	0.0184	0.0165	0.0144	0.0129	0.0
Medical	GQM	0.0087	0.0102	0.0123	0.0142	0.0135	0.0115	0.01	0.0087	0.0
	QPM	0.0086	0.0101	0.0122	0.0141	0.0134	0.0114	0.0098	0.0086	0.0

Table 9: MSE of absolute PCT moments when image is scaled to various sizes (first column). Second column represents the order of the moments taken for comparison. Range of v in all the cases is between 0 and 20.

PCT Size	u	ZOA	Lena GQM	QPM	ZOA	Logo GQM	QPM	ZOA	Medical GQM	QPM
48×48	0–20	0.122	0.1227	0.1182	0.4075	0.1812	0.1771	0.0587	0.4607	0.4621
80×80	0–20	0.0789	0.0452	0.0435	0.2477	0.0702	0.068	0.0386	0.203	0.2032
48×48	80–100	0.0552	0.0288	0.0142	0.1791	0.0923	0.0154	0.0224	0.0058	0.0035
80×80	80–100	0.0391	0.014	0.0129	0.1281	0.0168	0.0128	0.0156	0.004	0.0037

capacity of the PCT is weaker than the PCET. However, the MSE, SSIM, and FSIM of the PCT are comparable with the statistics of the PHFM, and hence the rotational invariance quality of the PCT is similar to the PHFM. As in the case of PCET and PHFM, the difference in moments when rotated at 90° is zero.

Table 9 shows MSE of the computed moments with two sizes of the image, when the image is scaled to 0.75 (size $= 48 \times 48$) and when yjr image is scaled to 1.25 (size $= 80 \times 80$). We observed that at both the sizes and $u = 0 - 20$, the MSE is largest among PCT, PCET, and PHFM, except for the medical image and ZOA method. Therefore, the scaling invariance at low moments is not as effective as in PCET and PHFM. However, we could not draw such conclusions for higher moments. We also noted that the MSE of the Lena and the logo is small in our algorithm as compared with the other two methods, indicating that the PCT moments with our method is supporting the scaling invariance better than the other two methods. In the medical image, the same conclusion can be drawn but at higher moments.

4.4. PST. Figure 7 shows reconstruction of images using the three algorithms. At first look, we note that in all the images, there is a black round spot at the center, which appear more prominent at lower moments. It is apparent from the figure that at low maximum order (0-20) for reconstruction, the three algorithms look similar with each other for all the three images. However, at higher maximum order (0-100) for reconstruction, the superiority of the GQM over the ZOA and the superiority of the QPM over the other two algo-

rithms are apparent. At higher maximum moments, white patches appear in the interior of the reconstructed image in the first rows in all the three images. Visually, the distinction between GQM and QPM is not clear.

Table 10 shows the MSE, SSIM, and the FSIM between the base images and the reconstructed images using PCT moments. The statistical analysis of the table supports Figure 7 with the fact that at lower moments, the reconstructed images looks similar in all the three methods. At moments with order 0-60, the superiority of the GQM and QPM over the ZOA is observed in the table. At moments with order 0-100, the image reconstructed using our method has the smallest MSE except the logo image, SSIM is largest in all the images, and except the medical image, FSIM is the largest in our method.

Table 11 shows the MSE for absolute moments between the base images and rotated images. At first sight, the table shows that the MSE in GQM and QPM have values similar across the table indicating that the two methods have similar rotational invariance property in all the three images. Both the algorithms have MSE smaller than the ZOA showing that both the methods have superior rotational invariance property than the ZOA method. As in the cases of other three moments, the difference in moments when rotated at 90° is zero.

Table 12 shows MSE of the computed moments with two sizes of the images, when the images are scaled to 0.75 (size $= 48 \times 48$) and when the images are scaled to 1.25 (size $= 80 \times 80$). We observed that at both the sizes and $u = 0 - 20$, the MSE is similar in GQM and QPM across the three images. However, $u = 80 - 100$, the MSE is smallest
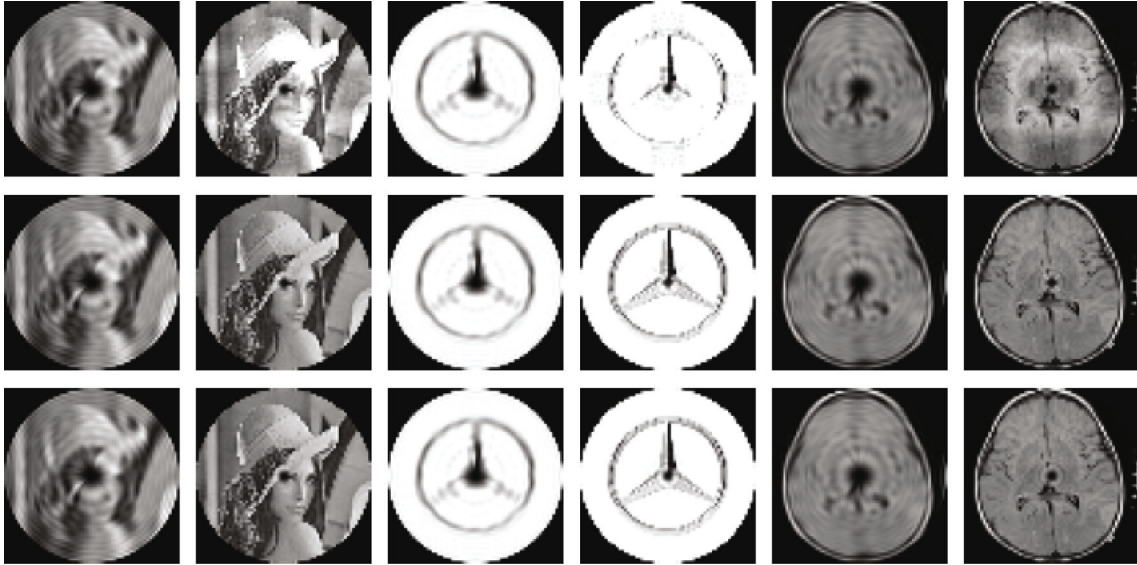
Figure 7: Reconstruction of image using PST with the three algorithms. The first row is reconstructed using the ZOA, the second row is reconstructed using the GQM, and the third row is reconstructed using the QPM. The first two columns correspond to the reconstructed Lena image using moments and repetitions 0-20 and 0-100, respectively. Similarly, the next two columns correspond to the reconstructed Logo image using moments and repetitions 0-20 and 0-100, respectively. And the last two columns correspond to the reconstructed medical image using moments and repetitions 0-20 and 0-100, respectively.

Table 10: MSE, SSIM, and FSIM between the base images and reconstructed images using PST moments. In columns 3-5, the images are reconstructed using orders 0-20 and repetition 0-20; in columns 6-8, the images are reconstructed using orders 0-60 and repetition 0-60; and in columns 9-11, the images are reconstructed using orders 0-100 and repetition 0-100. The first and second columns represent the images and algorithms, respectively, used for the reconstruction of the images.

| PST | | Maximum order 20 | | | Maximum order 60 | | | Maximum order 100 | | |
Image	Method	MSE	SSIM	FSIM	MSE	SSIM	FSIM	MSE	SSIM	FSIM
	ZOA	0.0449	0.7731	0.8728	0.0497	0.8911	0.9055	0.0918	0.8426	0.8887
Lena	GQM	0.045	0.7723	0.8726	0.0122	0.958	0.9645	0.0069	0.9792	0.9799
	QPM	0.045	0.7723	0.8726	0.0122	0.958	0.9645	0.0068	0.9801	0.9801
	ZOA	0.0228	0.768	0.8448	0.0116	0.8387	0.9098	0.0104	0.7866	0.8987
Logo	GQM	0.0228	0.7691	0.8454	0.0089	0.94	0.9409	0.0054	0.9569	0.9584
	QPM	0.0228	0.7691	0.8454	0.0089	0.9402	0.9409	0.0056	0.9598	0.959
	ZOA	0.0365	0.7599	0.9025	0.0444	0.8156	0.9354	0.1468	0.7484	0.8851
Medical	GQM	0.0373	0.7556	0.9009	0.0103	0.9496	0.9761	0.0056	0.9672	0.9865
	QPM	0.0373	0.7556	0.9009	0.0103	0.9495	0.9759	0.0055	0.9701	0.9861

Table 11: MSE between absolute values of moments of base images and rotated images using PST moments.

Image	Method	10°	20°	30°	40°	50°	60°	70°	80°	90°
	ZOA	0.0166	0.0191	0.022	0.0246	0.0266	0.023	0.02	0.0165	0.0
Lena	GQM	0.0087	0.0098	0.012	0.0148	0.0164	0.0129	0.0106	0.0086	0.0
	QPM	0.0087	0.0098	0.012	0.0148	0.0164	0.0129	0.0106	0.0086	0.0
	ZOA	0.0143	0.0163	0.0184	0.0228	0.0227	0.0183	0.0168	0.0147	0.0
Logo	GQM	0.0094	0.0108	0.0127	0.0159	0.0158	0.0124	0.0106	0.0094	0.0
	QPM	0.0093	0.0108	0.0127	0.0159	0.0158	0.0124	0.0106	0.0094	0.0
	ZOA	0.0129	0.0156	0.018	0.0206	0.0198	0.0173	0.0147	0.0126	0.0
Medical	GQM	0.0087	0.0104	0.0123	0.015	0.0141	0.012	0.0101	0.0084	0.0
	QPM	0.0087	0.0104	0.0123	0.015	0.0141	0.012	0.0101	0.0084	0.0

TABLE 12: MSE of absolute PST moments when image is scaled to various sizes (first column). The second column represents the order of the moments taken for comparison. The range of v in all the cases is between 0 and 20.

PST Size	u	Lena ZOA	GQM	QPM	Logo ZOA	GQM	QPM	Medical ZOA	GQM	QPM
48×48	0–20	0.1274	0.1227	0.1227	0.4265	0.1738	0.1738	0.0612	0.4385	0.4385
80×80	0–20	0.0801	0.0417	0.0417	0.2498	0.0677	0.0677	0.0395	0.1945	0.1944
48×48	80–100	0.0553	0.0366	0.0151	0.1818	0.0887	0.0123	0.0229	0.0067	0.0044
80×80	80–100	0.0399	0.0128	0.0133	0.1303	0.0135	0.013	0.0168	0.0038	0.0037

in both the scaled images, indicating the superiority of our method at higher moments across the three images at PST moments as well.

5. Conclusion

Due to a vast area of applications of image moments, their accurate computation is an important task. We have used here an analytic integration method mixed with numerical computations to compute moments at better accuracy compared to recent techniques used in the literature. We have used the technique for computing moments to a family of moments PCET, PCT, and PCET, known as PCET moments along with PHFT moments. We have compared their accuracy with simplified technique used in literature and an improved Gaussian quadrature integration technique and found that the method used in this paper is superior to both of them. The PHT and PHFT moments closely follow rotational invariance and scaling invariance. We found that the accuracy as well as the rotation invariance capabilities of the PCET and PHFT moments can be increased by using the method discussed in this paper. In PST and PCT, the rotation invariance statistics is similar to the other good method GQM. However, given the better accuracy of moments computed using QPM, the rotated image will have better moments in terms of accuracy when compared with the GQM. In many applications, accurate rotational invariant moments are required. Such studies will benefit from this method. For example, we showed the applicability of the moments in image reconstruct using three test images. One of the concerns for this method may be computational complexity. We have used four cores available mostly in modern laptops and computers to run the code in parallel with four threads. We found that using these four threads, the computational cost almost reduced four fold. In addition, the generation of the moments for various images does not require time in multiple folds. Only once a template for the moments needs to be computed. Once this template is ready, the template can be applied on any number of images to compute moments very quickly. In the future, research can be done to reduce the complexity of the algorithm.

The approach used in this paper can be utilized in multiple applications. In addition to image reconstruction and image watermarking, image moments can also be used in classification problems. Here, the various orders of image can be used to construct feature vector. The feature vector can be used independently or can be used as addition to other features of the image.

Data Availability

All the data used have been mentioned in the manuscript.

Conflicts of Interest

The authors declare that they have no conflict of interest.

References

[1] J. Flusser and T. S. B. Zitová, "Applications," *Moments and moment invariants in pattern recognition*, vol. 8, pp. 235–287, 2009.

[2] X. Liu, Y. Wu, Z. Shao, and J. Wu, "The modified generic polar harmonic transforms for image representation," *Pattern Analysis and Applications*, vol. 23, no. 2, pp. 785–795, 2020.

[3] B. Zitová and J. Flusser, "Image registration methods: a survey," *Image and Vision Computing*, vol. 21, pp. 977–1000, 2003.

[4] C. Clemente, L. Pallotta, D. Gaglione, A. De Maio, and J. J. Soraghan, "Automatic target recognition of military vehicles with krawtchouk moments," *IEEE Transactions on Aerospace and Electronic Systems*, vol. 53, no. 1, pp. 493–500, 2017.

[5] K. M. Hosny, M. M. Darwish, and T. Aboelenen, "New fractional-order legendre-fourier moments for pattern recognition applications," *Pattern Recognition*, vol. 103, article 107324, 2020.

[6] G. Xu, Y. Zhang, S. Ji, Y. Cheng, and Y. Tian, "Research on computer vision-based for UAV autonomous landing on a ship," *Pattern Recognition Letters*, vol. 30, pp. 600–605, 2009.

[7] T. Mostafa, H. M. Abbas, and A. A. Wahdan, "On the use of hierarchical color moments for image indexing and retrieval," in *IEEE International Conference on Systems, Man and Cybernetics*, Yasmine Hammamet, Tunisia, 2002.

[8] Y. Xin, S. Liao, and M. Pawlak, "Circularly orthogonal moments for geometrically robust image water-marking," *Pattern Recognition*, vol. 40, pp. 3740–3752, 2007.

[9] Y. Xin, M. Pawlak, and S. Liao, "Accurate computation of Zernike moments in polar coordinates," *IEEE Transactions on Image Processing*, vol. 16, no. 2, pp. 581–587, 2007.

[10] C. Singh and R. Upneja, "A computational model for enhanced accuracy of radial harmonic Fourier moments," in *World Congress of Engineering*, pp. 1189–1194, UK, World congress of engineering, London, UK, London, 2012.

[11] L. Li, S. Li, A. Abraham, and J. S. Pan, "Geometrically invariant image watermarking using polar harmonic transforms," *Information Sciences*, vol. 199, pp. 1–19, 2012.

[12] K. M. Hosny and M. M. Darwish, "A kernel-based method for fast and accurate computation of PHT in polar coordinates," *Journal of Real-Time Image Processing*, vol. 16, no. 4, pp. 1235–1247, 2019.

[13] B. Ma, L. Chang, C. Wang, J. Li, X. Wang, and Y. Q. Shi, "Robust image watermarking using invariant accurate polar harmonic Fourier moments and chaotic mapping," *Signal Processing*, vol. 172, article 107544, 2020.

[14] B. Mahdian and S. Saic, "Detection of copy–move forgery using a method based on blur moment invariants," *Forensic Science International*, vol. 171, pp. 180–189, 2007.

[15] J. Flusser and T. S. B. Zitová, "Introduction to moments," in *Moments and Moment Invariants in Pattern Recognition*, pp. 1–11, Wiley, 2009.

[16] C. Teh and R. T. Chin, "On image analysis by the methods of moments," *IEEE Transactions on Pattern Analysis and Machine Intelligence*, vol. 10, no. 4, pp. 496–513, 1988.

[17] R. Mukundan, S. H. Ong, and P. A. Lee, "Image analysis by tchebichef moments," *IEEE Transactions on Image Processing*, vol. 10, no. 9, pp. 1357–1364, 2001.

[18] Y. Sheng and L. Shen, "Orthogonal Fourier–Mellin moments for invariant pattern recognition," *Journal of the Optical Society of America. A*, vol. 11, no. 6, pp. 1748–1757, 1994.

[19] C. Wang, X. Wang, Z. Xia, B. Ma, and Y. Shi, "Image description with polar harmonic Fourier moments," *IEEE Transactions on Circuits and Systems for Video Technology*, vol. 30, no. 12, pp. 4440–4452, 2020.

[20] M. R. Teague, "Image analysis via the general theory of moments," *Journal of the Optical Society of America A*, vol. 70, pp. 920–930, 1980.

[21] K. M. Hosny, H. M. Hamza, and N. A. Lashin, "Copy-move forgery detection of duplicated objects using accurate pcet moments and morphological operators," *Imaging Science Journal*, vol. 66, no. 6, pp. 330–345, 2018.

[22] J. Wang, G. Wang, M. Li, and W. Du, "Hand vein recognition based on PCET," *Optik*, vol. 127, pp. 7663–7669, 2016.

[23] S. P. Singh, S. Urooj, and A. Lay-Ekuakille, "Breast cancer detection using PCPCET and ADEWNN: a geometric invariant approach to medical x-ray image sensors," *IEEE Sensors Journal*, vol. 16, no. 12, pp. 4847–4855, 2016.

[24] S. Gishkori and B. Mulgrew, "Pseudo-Zernike moments based sparse representations for SAR image classification," *IEEE Transactions on Aerospace and Electronic Systems*, vol. 55, no. 2, pp. 1037–1044, 2019.

[25] Y. Kumar, A. Aggarwal, S. Tiwari, and K. Singh, "An efficient and robust approach for biomedical image retrieval using Zernike moments," *Biomedical Signal Processing and Control*, vol. 39, pp. 459–473, 2018.

[26] M. K. Singh, S. Kumar, M. Ali, and D. Saini, "Application of a novel image moment computation in X-ray and MRI image watermarking," *IET Image Processing*, vol. 15, no. 3, pp. 666–682, 2021.

[27] M. Pawlak, G. S. Panesar, and M. Korytkowski, "A novel method for invariant image reconstruction," *Journal of Artificial Intelligence and Soft Computing Research*, vol. 11, no. 1, pp. 69–80, 2021.

[28] C. Wang, Q. Hao, B. Ma, J. Li, and H. Gao, "Fractional-order quaternion exponential moments for color images," *Applied Mathematics and Computation*, vol. 400, article 126061, 2021.

[29] C. Wang, Q. Hao, B. Ma et al., "Octonion continuous orthogonal moments and their applications in color stereoscopic image reconstruction and zero-watermarking," *Engineering Applications of Artificial Intelligence*, vol. 106, article 104450, 2021.

[30] Z. Wang, A. C. Bovik, H. R. Sheikh, and E. P. Simoncelli, "Image quality assessment: from error visibility to structural similarity," *IEEE Transactions on Image Processing*, vol. 13, no. 4, pp. 600–612, 2004.

[31] L. Zhang, L. Zhang, X. Mou, and D. Zhang, "FSIM: a feature similarity index for image quality assessment," *IEEE Transactions on Image Processing*, vol. 20, no. 8, pp. 2378–2386, 2011.

[32] K. M. Hosny and M. M. Darwish, "Invariant image watermarking using accurate polar harmonic transforms," *Computers & Electrical Engineering*, vol. 62, pp. 429–447, 2017.